J. Cent. South Univ. (2022) 29: 3870−3883
DOI: https://doi.org/10.1007/s11771-023-5243-6

Springer

Fabrication of triangular Cu_3P nanorods on Cu nanosheets as electrocatalyst for boosted electrocatalytic water splitting

DANG Rui(党蕊)[1]*, XU Xiu-feng(徐秀凤)[1, 2], XIE Meng-meng(谢蒙蒙)[1, 2]

1. Northwest Institute For Nonferrous Metal Research, Xi'an 710016, China;
2. The Faculty of Printing, Packaging Engineering and Digital Media Technology, Xi'an University of Technology, Xi'an 710054, China

Abstract: Non-precious electro catalysts with high-efficiency, cheapness and stablility are of great significance to replace noble metal electro catalysts in the hydrogen evolution reaction (HER) and oxygen evolution reaction (OER). In this work, triangular Cu@CuO nanorods on Cu nanosheets were fabricated by a novel in-situ oxidation approach using Cu nanosheets as self-template and conductive nano-substrate in an aqueous solution of $NaOH/H_2O_2$, and then by low-temperature phosphorization treatments. The experimental results show that the phosphating temperature has a significant effect on the morphology, composition and number of active sites of $Cu@Cu_3P$ nanorods. The $Cu@Cu_3P$-280 electrode exhibits a good HER catalytic activity of achieving a current density of 10 mA/cm^2 at 252 mV in acid electrolyte. After catalysis for 14 h, the current density can still reach 72% of the initial value. Moreover, the $Cu@Cu_3P$-280 electrode also shows an excellent OER catalytic activity in basic electrolyte, reaching a current density of 10 mA/cm^2 at the overpotential value of 200 mV. After catalysis for 12 h, the current density remained more than 93% of the initial value. This work provides a theoretical basis for the directional design and preparation of sustainable, low-cost, bifunctional electrocatalytic materials.

Key words: $Cu@Cu_3P$; electrocatalysis; oxygen evolution reaction; hydrogen evolution reaction

Cite this article as: DANG Rui, XU Xiu-feng, XIE Meng-meng. Fabrication of triangular Cu_3P nanorods on Cu nanosheets as electrocatalyst for boosted electrocatalytic water splitting [J]. Journal of Central South University, 2022, 29(12): 3870−3883. DOI: https://doi.org/10.1007/s11771-023-5243-6.

1 Introduction

In recent decades, the energy donors are dominated mainly by fossil fuels, which offer some benefits, but bring about such issues as environmental pollution, greenhouse effect and resource depletion. In order to meet the ever-increasing energy demand, a great deal of efforts have been put into exploiting new clean and highly efficient energy conversion technologies via electrocatalytic reaction in recent years. Electrocatalytical water splitting has been widely regarded as the most promising and sustainable technology for green hydrogen fuel production from aqueous solution [1 − 6]. The efficiency of electrochemical hydrogen production is determined by the activity of the electrocatalyst in water splitting reactions. Although the Pt-group metals and Ru- or Ir-based compounds are considered the most active catalyst for the hydrogen evolution reaction (HER) and oxygen evolution reaction (OER) [7 − 11], respectively, the high cost and scarcity significantly prohibit their large scale and

Foundation item: Project(21905232) supported by the National Natural Science Foundation of China
Received date: 2022-08-04; **Accepted date:** 2022-10-24
Corresponding author: DANG Rui, PhD, Senior Engineer; E-mail: dr0501@163.com; ORCID: https://orcid.org/0000-0003-0017-6850

practical application. Furthermore, it is urgent to develop a new type of effective HER and OER electrocatalyst with low cost and high abundance.

Transition metal phosphides are of great interest as inexpensive alternatives to precious metal catalysts owing to their appealing conductivity, chemical stability and excellent catalytic performance for HER and OER. The extensively investigated metal phosphides include Ni_2P [12−14], FeP [15−16], MoP [17−18], Co_2P [19−21], NiCuP [22], NiCoP [23], Cu_3P [24], WP_2 [25−28], etc. All of them show comparable electrocatalytic performances to noble metals catalysts. Nevertheless, as an earth abundant transition metal, Cu-based catalysts have relatively fewer studies in terms of HER and OER properties.

Copper phosphide (Cu_3P) is a candidate for energy conversion and storage technologies because of its favorable electronic structure, combined with low cost and thermal stability [29−30]. However, Cu_3P is prone to agglomeration of active sites during the catalytic process, and part of the catalyst will be lost, thus affecting the catalytic activity. Recent reports have proved that nanocatalysts loaded or grown on the conductive substrate reveal better catalytic performance than pure catalysts. For instance, ZHOU et al [31] reported Cu_3P nanowires on Cu foam via a simple two-step method. The Cu_3P nanowires/copper foam (NWs/CF) exhibits enhanced activity toward OER with a small overpotential of 327 mV at the current density of 20 mA/cm^2, and good durability in alkaline medium. TIAN et al [32] reported self-supported Cu_3P nanowires arrays on porous copper foam. Owing to the unique structure and composition, Cu_3P NW/CF maintains its HER activity for at least 25 h and the catalytic current density can approach 10 mA/cm^2 at an overpotential of 143 mV. CUI et al [33] reported Cu_3P nanobush (NB) on copper meshes, demonstrating that the Cu_3P NB/Cu exhibits a superior catalytic HER activity of achieving a current density of 10 mA/cm^2 at 120 mV and exhibits a long-term stability in acid solutions. Although with such success, the substrates are concentrated on bulk materials such as copper foam and nickel foam, while micro-nano conductive materials are rarely reported.

Herein, we report on our recent efforts in developing a novel self-supported triangular Cu_3P nanorods on conductive substrate of Cu nanosheets by topotactic conversion from its Cu@CuO nanorod precursor. The triangular Cu@CuO nanorod was directly grown on Cu nanosheet by a novel in-situ oxidation method, then followed by low-temperature phosphidation reaction. Benefiting from the structural and component merits, the as-prepared triangular Cu@Cu_3P nanorods exhibit enhanced catalytic performance for HER and OER, respectively. The triangular Cu@Cu_3P nanorods exhibit high HER activity of achieving a current density of 10 mA/cm^2 at 252 mV and displays a long-term stability in acid solution. This catalyst displays a high catalytic activity in basic electrolytes, reaching a current density of 10 mA/cm^2 at the overpotential value of 200 mV for OER. This work provides a useful strategy for developing efficient micro-nano self-supporting catalysts with high conductivity and numerous reactive sites for HER and OER, which encourages more research on other similar electrocatalysts for renewable energy. We expect that this facile synthetic strategy could be expanded to synthesize many other phosphides.

2 Experimental

2.1 Preparation of electrocatalysts

2.1.1 Cu nanosheets

The well-defined Cu nanosheets were prepared according to the procedures in our previous report [34]. In brief, 1.0 g $C_6H_{12}O_6·H_2O$, 0.5 g polyvinyl pyrrolidone (PVP) and $CuSO_4$ were dissolved into 25 mL of deionized water with magnetic stirring vigorously, then the mixture was transferred into a Teflon-lined autoclave and heated at 180 ℃ for 3 h.

2.1.2 Triangular CuO nanorods on Cu nanosheets

The triangular CuO nanorods on Cu nanosheets (Cu@CuO nanorods) were synthesized by a simple hydrothermal process. In the typical synthesis, an amount of Cu nanosheets was dispersed in 4.2 mL of NaOH (0.6 mol/L) in a Teflon-lined vessel with magnetic stirring vigorously. Then, 5 mL H_2O_2 (30%) was injected rapidly into the mixture solution under stirring. Afterward, the vessel was sealed and then hydrothermally heated at 120 ℃ for 11 h. The resulting precipitate was separated and washed with deionized water, and eventually dried in vacuum at

60 ℃ for 12 h.

2.1.3 Triangular Cu_3P nanorods on Cu nanosheets

The triangular Cu_3P nanorods on Cu nanosheets (Cu@Cu_3P nanorods) catalysts were synthesized through phosphorization procedure using the as-prepared triangular Cu@CuO nanorods as precursors. Typically, the as-prepared triangular Cu@CuO nanorods (0.1 g) and NaH_2PO_2 (0.25 g) were placed at two different locations of the tube furnace with NaH_2PO_2 at the upstream side. After being flushed with Ar, the center of the furnace was elevated to 280 ℃ at a heating rate of 5 ℃/min and maintained at this temperature for 60 min. To investigate the impact of the phosphating temperature on the electrocatalytic activity, the phosphorization process was conducted at 270 ℃ and 300 ℃, whereas the other parameters remained unchanged.

2.1.4 Cu/Cu_3P nanosheets

For comparison, the samples directly phosphatized with Cu nanosheets were synthesized by the following steps. The as-prepared Cu nanosheets (0.1 g) and NaH_2PO_2 (0.25 g) were placed at two different locations of the tube furnace with NaH_2PO_2 at the upstream side. After being flushed with Ar, the center of the furnace was elevated to 280 ℃ at a heating rate of 5 ℃/min and maintained at this temperature for 60 min.

2.2 Electrochemical measurements

All electrochemical tests were performed at room temperature with CHI 660D electrochemical workstation. The performances of HER and OER were tested with a standard three-electrode system. The as-prepared catalysts, Ag/AgCl electrode, Pt sheet and graphite rod were chosen as working electrode, reference electrode, and counter electrode, respectively. The electrocatalytic activities of catalysts for HER and OER were measured in 0.5 mol/L H_2SO_4 and 1 mol/L KOH solution, respectively. In all measurements, the Ag/AgCl reference electrode was calibrated with respect to reversible hydrogen electrode (RHE). All the potentials reported were versus the RHE according to $E_{vsRHE}=E_{vsAg/AgCl}+E^{\ominus}_{vsAg/AgCl}+0.059$ pH. The LSV was recorded at a scan rate of 5 mV/s and the corresponding Tafel plots were used to evaluate the catalytic kinetics. Impedance measurements were carried out with frequency ranged from 0.1 Hz to 10 kHz under the amplitude of 10 mV. The effective electrochemical surface area (ECSA) was determined from the C_{dl} of the catalyst surface. The C_{dl} was determined by measuring CVs with multiple scan rates in non-faradaic potential region.

3 Results and discussion

The typical procedure for synthesis of triangular Cu@Cu_3P nanorod is summarized in Scheme 1. In brief, Cu nanosheets were firstly synthesized according to hydrothermal method. Then, Cu nanosheets as both self-template and nano conductive substrate were immersed in the solution of $NaOH/H_2O_2$ for the formation of triangular Cu@CuO nanorod. Followed by a low-temperature phosphorization process, the triangular Cu@CuO nanorod was successfully converted to triangular Cu@Cu_3P nanorod, using NaH_2PO_4 as phosphourus source.

The SEM image shows that the Cu nanosheets display a plate-shaped morphology with smooth surface and has large area characteristic of 30 − 100 μm in diameter (Figures 1(a) and S1). The as-prepared Cu nanosheet was employed as self-template and conductive substrate in the following process to prepare triangular CuO nanorods materials. Figure 1(b) shows the SEM image of the triangular CuO nanorods grown on Cu nanosheets, in which the entire surface of the Cu nanosheet is covered uniformly by densely packed CuO nanorods (Figure S2). A close view of such nanorod (Figure 1(c)) reveals that the structure of nanorod is triangular column, and extends vertically from the Cu nanosheets with thickness of 200 − 500 nm and

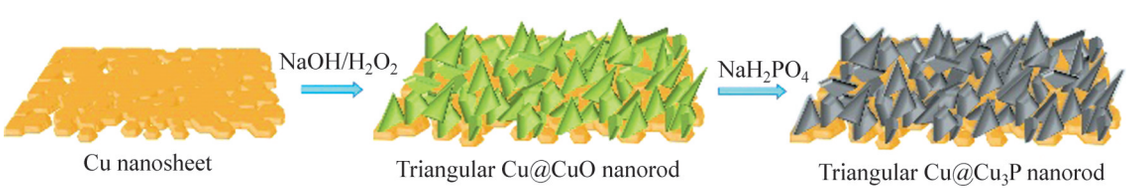

Scheme 1 Synthesis procedure of the triangular Cu@Cu_3P nanorod

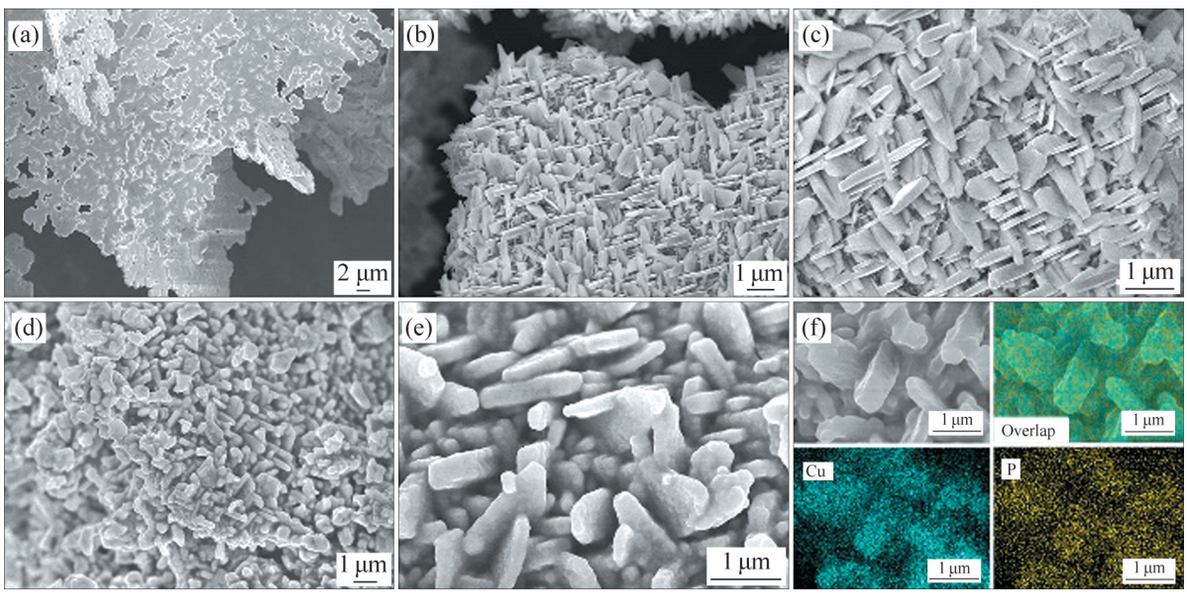

Figure 1 SEM images (a−e) and EDX distribution mapping (f) in triangular Cu@Cu_3P nanorods: (a) Cu nanosheets; (b−c) Triangular Cu@CuO nanorods; (d−e) Triangular Cu@Cu_3P nanorods; (f) EDX element distribution mappings of Cu, P and overlap of elements in triangular Cu@Cu_3P nanorods

length of 1−3 μm. After the phosphorization process through a gas-solid reaction, the morphology of triangular nanorods was preserved (Figure 1(d)). Meanwhile, the surfaces of triangular Cu_3P nanorods became rough and thick, thus improving the surface area and active sites, resulting in the enhanced catalytic activity (Figure 1(e)). The SEM and corresponding elemental mapping patterns of Cu and P for the triangular Cu_3P nanorods in Figure 1(f), clearly reveal that Cu and P were uniformly distributed on the nanorods, which further confirms the successful chemical conversion of Cu@CuO to Cu@Cu_3P.

The crystalline phases were measured by XRD. Figure 2(a) shows the XRD patterns of as-synthesized Cu nanosheets, Cu@CuO nanorods and Cu@Cu_3P nanorods. It can be seen that all the samples present three strong diffraction peaks at 43.4°, 50.6° and 74.4°, which can be assigned to (111), (200) and (220) crystal planes of face-centered cubic structure due to the Cu nanosheet substrate (PDF #04-0836). After the oxidation treatments, a series of new diffraction peaks can be observed, which well correspond to the crystal plane of the CuO (PDF #48-1548). After low-temperature phosphorization process, the diffraction peaks located at 28.6°, 36.2°, 39.4°, 41.8°, 45.1°, 46.5°, 47.3°, 52.5°, 53.4°, 56.4°, 59° and 66.5° corresponding well to the (111), (112), (202), (221), (300), (113), (212), (220), (221), (311), (222) and (223) planes of the Cu_3P (PDF #12-1263). No other XRD peak except Cu_3P crystal form was observed, demonstrating that the triangular Cu@Cu_3P nanorod structrue was successfully obtained. Figure 2(b) presents the TEM image of Cu@Cu_3P nanorods, thus showing that the structure of triangular nanorod was retained after phosphating. The HRTEM image (Figure 2(c)) confirms that the Cu_3P nanorod has an interplane distance of the lattice fringe of 0.23 nm, which corresponds to the (202) facet of Cu_3P.

XPS spectrum was used to investigate the surface chemical composition and element valence states of the triangular Cu@Cu_3P nanorods. The full survey XPS spectrum in Figure 3(a) shows that the Cu@Cu_3P is composed of Cu, P, O and C elements.

Figure 3(b) shows the high-resolution XPS spectrum of Cu 2p. Two apparent peaks located at 932.6 and 934.3 eV originating from the Cu $2p_{3/2}$ species, and two additional peaks at 952.6 and 954.1 eV are corresponding to the Cu $2p_{1/2}$ species. The peaks at 932.6 and 952.6 correspond to the $Cu^{\delta+}$ $2p_{3/2}$ and $Cu^{\delta+}$ $2p_{1/2}$ in Cu_3P and the binding energies of 934.3 and 954.1 eV correspond to the Cu 2p peaks in oxidized copper [35 − 39]. The satellite peaks at 944.2 and 963.0 eV also show the existence of oxidation state of copper. There is no

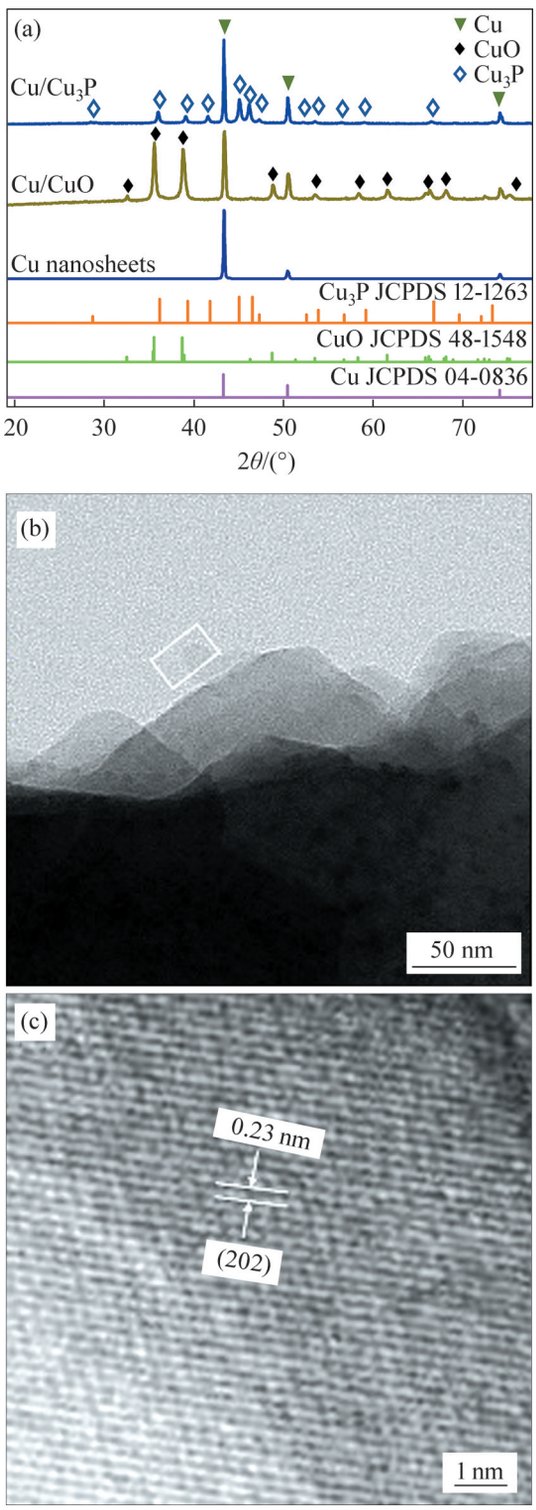

Figure 2 (a) XRD patterns of Cu nanosheet, Cu@CuO nanorod, Cu@Cu_3P nanorod, (b) TEM and HRTEM (c) images of triangular Cu@Cu_3P nanorods

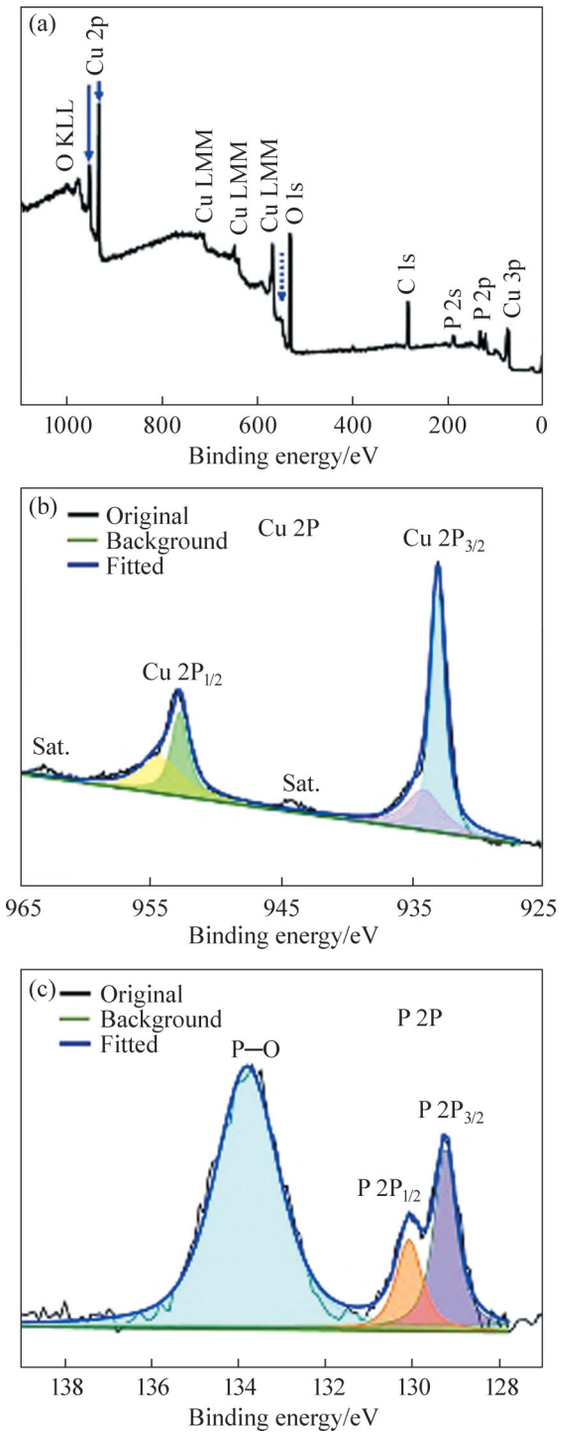

Figure 3 XPS survey spectrum of triangular Cu@Cu_3P nanorods (a), high-resolution XPS spectra of Cu 2p (b) and P 2p (c) for triangular Cu@Cu_3P nanorods

peak assigned to metal Cu, implying that Cu_3P nanorods have completely covered the surface of Cu nanosheets. Figure 3(c) shows that the peaks of the P 2p are located at 129.1 and 130.0 eV, corresponding to the P $2p_{3/2}$ and P $2p_{1/2}$, respectively, which are the characteristic peaks of P in Cu_3P [40−41]. In addition, the peak located at 133.6 eV can be assigned to P—O bands, which is probably due to the surface oxidation of Cu_3P after being exposure to air [42].

The morphology of the precursor Cu@CuO has a significant impact on the morphology of the final product. Therefore, the influence of the volume of H_2O_2 on morphology of as-prepared nanostructure was investigated, as shown in Figure 4.

Without adding H_2O_2 solution, the products with small amounts of flakes are grown on the surface of Cu nanosheets (Figure 4(a)), and most of the copper nanosheets are still partially exposed, indicating that the oxygen released by H_2O_2 plays an important role in the growth of CuO nanorods. With volume of H_2O_2 increased to 1 mL, the density of CuO grown on the surface of Cu nanosheets was also increasing (Figure 4(b)). When the volume of H_2O_2 reached 3 mL, part of the thin sheet began to grow into thick columnar structures (Figure 4(c)). Until the volume of H_2O_2 solution was 5 mL, triangular Cu@CuO nanorod material was obtained. However, when the volume of H_2O_2 further increased to 7 mL, the density of CuO on the surface of Cu nanosheet decreased although it presented the morphology of triangular nanorods (Figure 4(d)). This may be due to the excessive addition of H_2O_2 solution, which will neutralize part of the alkalinity of NaOH, resulting in reduced pH value in the solution and affecting the growth of the product.

The influence of the concentration of NaOH solution on the morphology of as-prepared nanostructure was likewise studied, as shown in Figure 5. Without adding NaOH solution, a large number of nanoparticles were grown on the surface of Cu nanosheets, which means that the structure of nanorods cannot be obtained simply by adding H_2O_2 solution (Figure 5(a)). When the concentration of NaOH was 0.1 mol/L, the triangular column structure began to appear, but the length of the nanorods is shorter (Figure 5(b)). With the increasing concentration of NaOH solution, the length of the nanorods also began to grow, as shown in Figure 5(c). When the concentration of NaOH was 0.8 mol/L, in addition to the formation of Cu@CuO nanorods, some multi-layered CuO nanoplates were formed in the product, which is mainly due to the rapid release of copper ions from Cu nanosheets, resulting in the generation of self-nucleating samples.

Based on the experiment results, it can be clearly seen that H_2O_2 and NaOH played a vital role

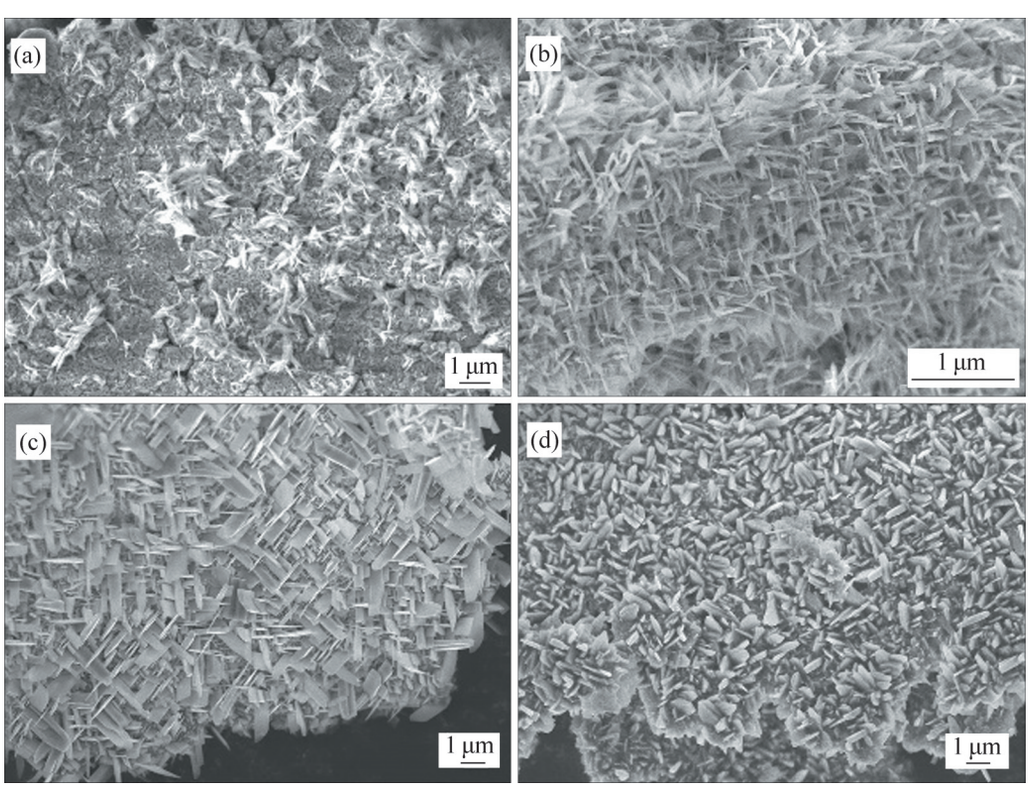

Figure 4 SEM images of Cu@CuO nanorods in solution with different H_2O_2 volumes: (a) Without H_2O_2; (b) 1 mL; (c) 3 mL; (d) 7 mL

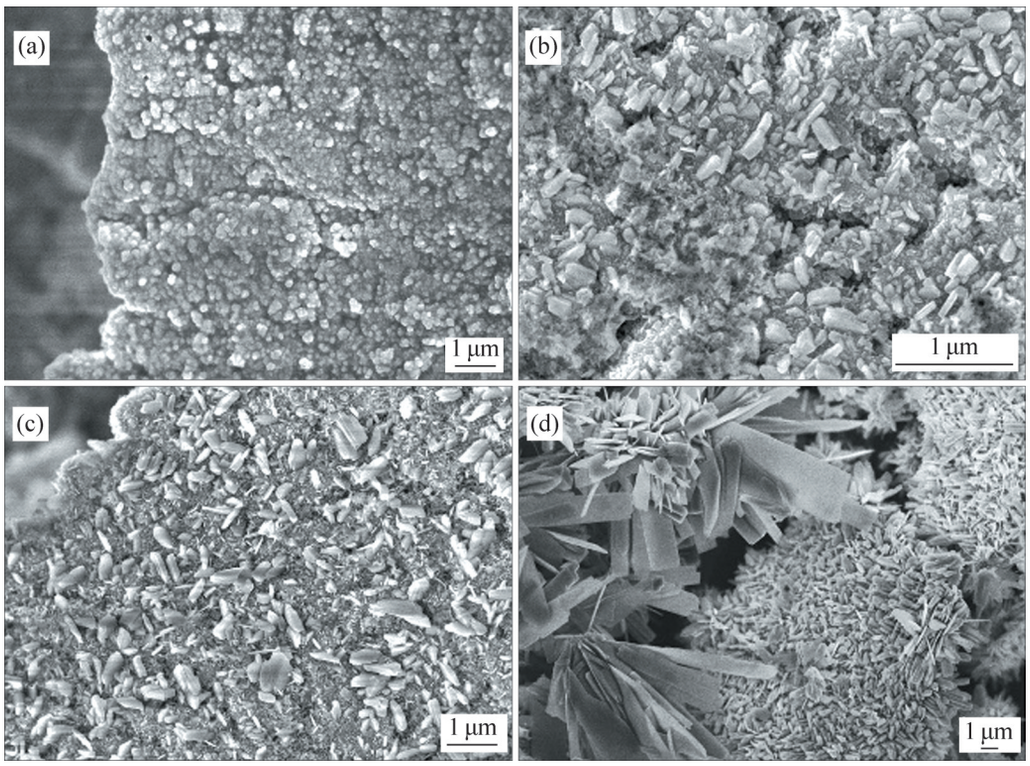

Figure 5 SEM images of Cu@CuO nanorods in different concentration of NaOH solution: (a) Without NaOH; (b) 0.1 mol/L; (c) 0.3 mol/L; (d) 0.8 mol/L

in the generation of precursor triangular Cu@CuO nanorods. As conductive substrate and self-template, Cu nanosheets can be dissolved at high temperature to produce Cu^{2+} ions acting as copper source. In the presence of H_2O_2 solution, the gas of oxygen was produced, which acts with NaOH solution to form the triangular Cu@CuO nanorods. Without adding H_2O_2 solution, the Cu^{2+} ions combine with OH^- ions to form $Cu(OH)_2$ at a slower reaction rate. In the absence of NaOH solution, Cu was oxidized by oxygen to obtain nanoparticles, but the morphology of nanorods could not be obtained.

For comparison, the samples phosphated at different temperatures and the samples directly phosphated with copper nanosheets were synthesized by the same procedure. The morphologies and crystal structures of the products were characterized by SEM and XRD, as shown in Figure 6. When the phosphating temperature was 270 ℃, the morphology of the sample did not change significantly compared with the CuO nanorods, and only the surface became rough (Figure 6(a)). The corresponding XRD pattern shows that the diffraction peaks of Cu, CuO and Cu_3P appeared simultaneously (Figure 6(b)), which confirmed that a small part of CuO was still not completely phosphatized at a low phosphating temperature, and the product was named Cu@CuO/Cu_3P-270 nanorods. Until the phosphating temperature reached 300 ℃, the surface of nanorods became rougher and all peaks of XRD pattern could be assigned to Cu and Cu_3P (Figures 6(c) and (d)). The results show that the intensity of the copper peak became weaker, which proved that part of the substrates of Cu nanosheets were involved in the phosphating reaction.

As a comparison, the pure Cu nanosheets were directly phosphated at 280 ℃ (Cu/Cu_3P nanosheet), and the morphology and crystal structure of products were characterized, as shown in Figures 6(e) and (f). The surface of copper nanosheets has changed from smooth to uneven, but no nanorod structure appeared (Figure 6(e)). The corresponding XRD pattern (Figure 6(f)) confirmed that the surface of the Cu nanosheet participated in the phosphating reaction, and part of Cu nanosheet was converted to Cu_3P.

To evaluate the electrocatalytic activities of

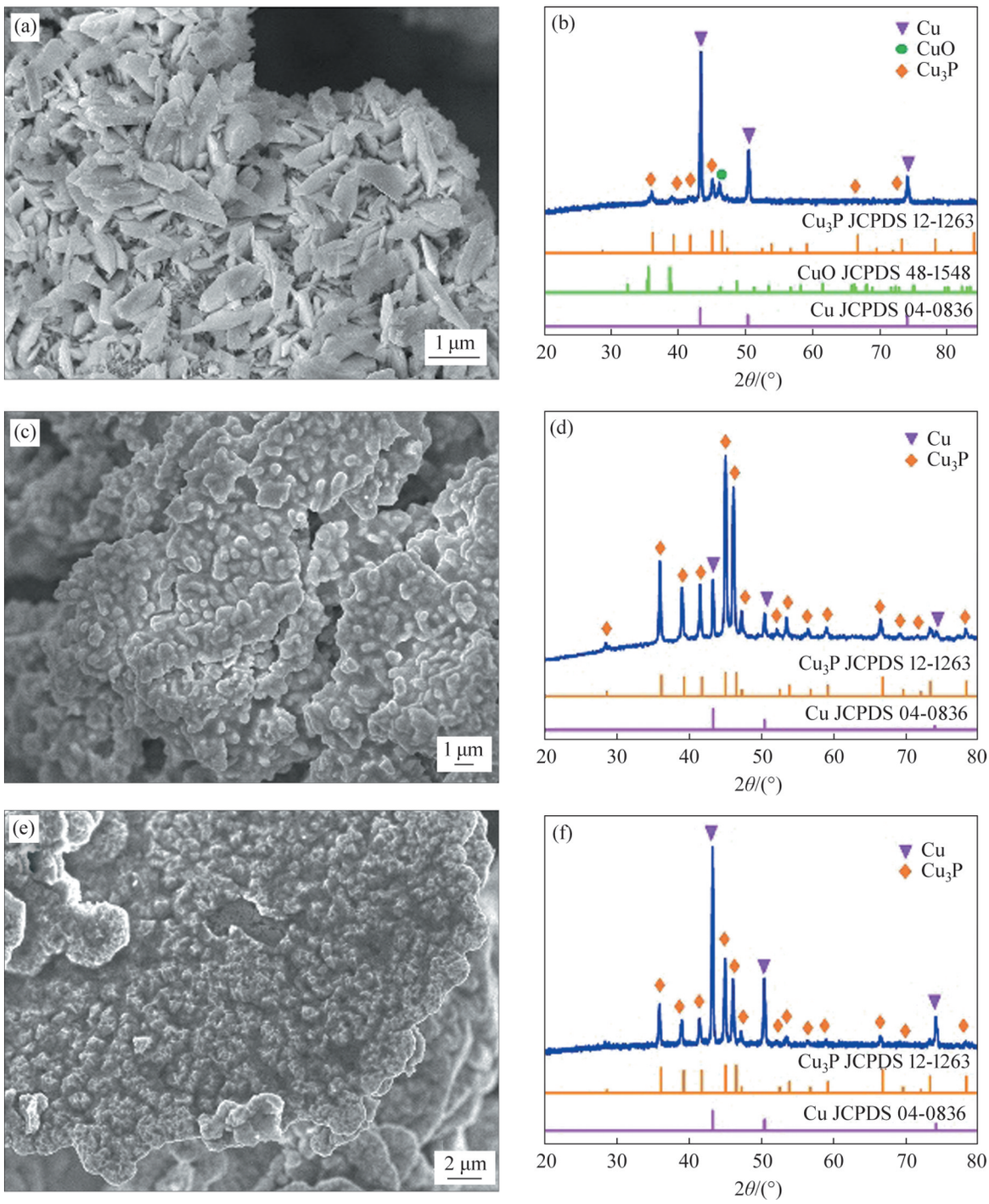

Figure 6 SEM images (a, c, e) and XRD patterns (b, d, f) of Cu@Cu_3P nanorods and nanosheets at different phosphating temperature: (a, b) Cu@Cu_3P nanorods, 270 ℃; (c, d) Cu@Cu_3P nanorods, 300 ℃; (e, f) Cu/Cu_3P nanosheets, 28 ℃

triangular Cu@Cu_3P-280 nanorods, HER and OER were measured. The catalytic activity of triangular Cu@Cu_3P-280 nanorods for HER was tested in a standard three-electrode system with 0.5 mol/L H_2SO_4 electrolyte. For comparison, the reference samples, including Cu@Cu_3P-300, direct phosphating of Cu nanosheets (Cu/Cu_3P NS) and Cu nanosheet, were also measured without iR correction in this study, as shown in Figure 7(a). The triangular Cu@Cu_3P-280 nanorod displayed a good HER catalytic performance with a low overpotential of 252 mV to reach a current density of 10 mA/cm^2, which is much smaller than that of Cu@Cu_3P-300 (272 mV), Cu/Cu_3P NS (433 mV) or Cu NS (542 mV). More importantly, an overpotential of 422 mV is required for the

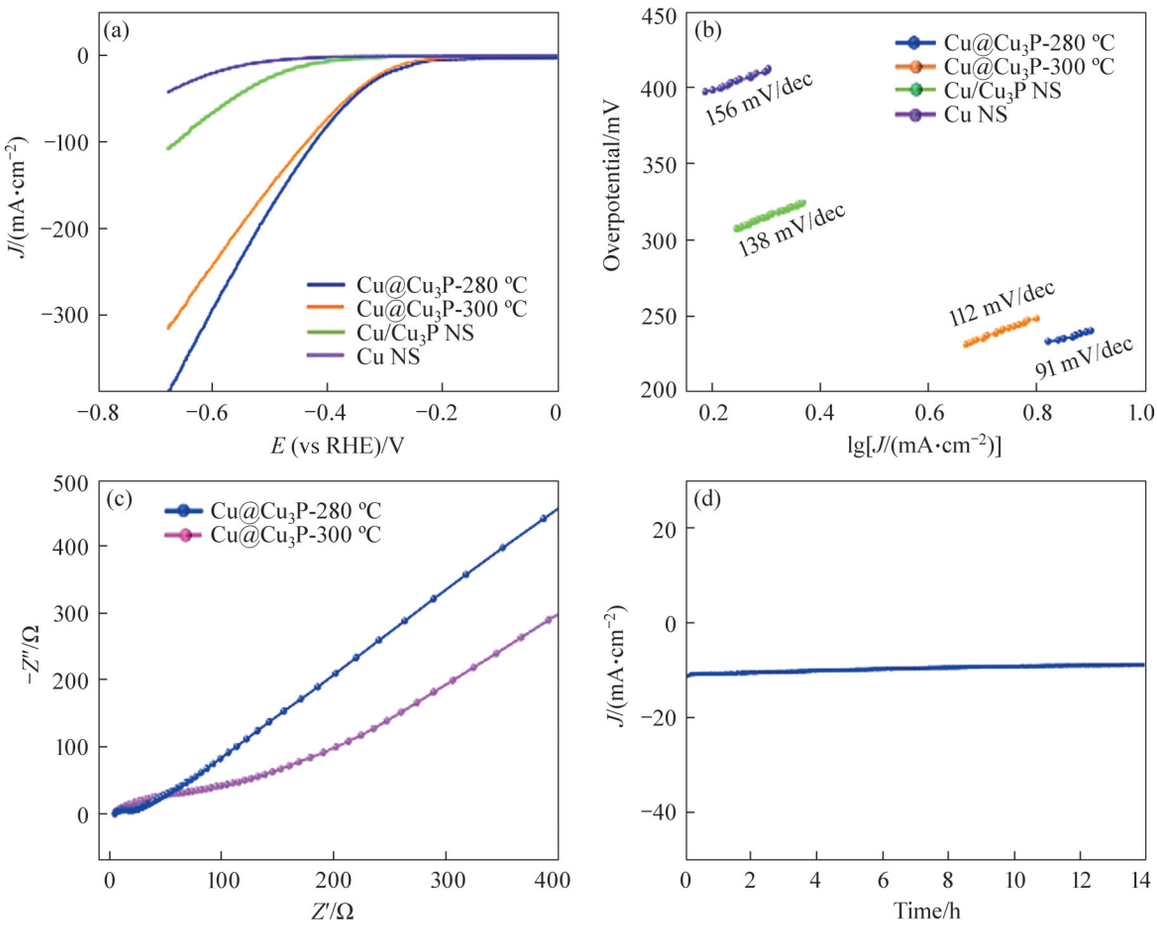

Figure 7 Electrocatalytic activity of the as-prepared triangular Cu@Cu_3P nanorods electrode for HER in 0.5 mol/L H_2SO_4: (a) Polarization curves; (b) Tafel plots; (c) EIS Nyquist plots; (d) Current density curve related to time at 10 mA/cm^2

triangular Cu@Cu_3P-280 nanorod to reach the current density of 100 mA/cm^2, which is lower than that of Cu@Cu_3P-300 (439 mV) or Cu/Cu_3P NS (664 mV). While, the polarization curve of Cu@CuO/Cu_3P-270 in 0.5 mol/L H_2SO_4 was also examined for comparison, as shown in Figure S3. From the results, HER performance of Cu@CuO/Cu_3P-270 is worse than that of Cu@Cu_3P-280 or Cu@Cu_3P-300.

The Tafel slopes for all electrocatalysts were further tested to gain an insight into the HER kinetics of the triangular Cu@Cu_3P nanorod (Figure 7(b)). The Tafel slope of 91 mV/dec for the triangular Cu@Cu_3P-280 nanorod electrode is lower than that of Cu@Cu_3P-300 (131 mV/dec), Cu/Cu_3P NS (138 mV/dec) or Cu NS (156 mV/dec), implying that a more rapid HER rate can be obtained in future industrial application when using the triangular Cu@Cu_3P-280 nanorod as an electro catalyst. Electrochemical impedance spectroscopy (EIS) measurements revealed that triangular Cu@Cu_3P-280 nanorod has a much smaller impedance, further confirming that its HER kinetics is faster than Cu@Cu_3P-300 nanorod (Figure 7(c)). The long-term stability of an electrode is another important issue to consider for practical application. The durability of triangular Cu@Cu_3P-280 nanorod is examined at 10 mA/cm in acid solution, as shown in Figure 7(d). The time-dependent current density only exhibits a slight decrease after 14 h, which reveals the excellent stability in the electrocatalytic process of this triangular nanorod.

The OER activities of the triangular Cu@Cu_3P-280 nanorod were also evaluated by using a typical three-electrode system in 1 mol/L KOH solution without iR drop compensation. All the potentials are relative to the reversible hydrogen electrode (RHE). Cu@Cu_3P-300, Cu NS and Cu/Cu_3P NS were

investigated under the same condition. Polarization curves of the samples obtained through the LSV measurements are presented in Figure 8(a). To reach a current density of 10 mA/cm^2, triangular Cu@Cu_3P-280 nanorod needs an overpotential of 200 mV, which is smaller than that of Cu@Cu_3P-300 nanorod (281 mV), Cu/Cu_3P NS (386 mV) or Cu NS (561 mV). At higher current density of 30 mA/cm^2, triangular Cu@Cu_3P-280 nanorod exhibited an overpotential of 390 mV, followed by Cu@Cu_3P-300 nanorod (η_{30}=492 mV) and Cu/Cu_3P NS (η_{30}=530 mV). The corresponding Tafel slopes are shown in Figure 8(b), the Tafel slope of triangular Cu@Cu_3P-280 nanorod is 170 mV/dec, which is lower than that of Cu@Cu_3P-300 nanorod (191 mV/dec), Cu/Cu_3P NS (292 mV/dec) or Cu NS (331 mV/dec), implying the most favorable catalytic kinetics toward OER. Additionally, the ECSA was evaluated through testing double-layer capacitance (C_{dl}). The C_{dl} values of triangular Cu@Cu_3P-280 nanorod and Cu/Cu_3P NS are 17.8 and 1.38 mF cm^{-2}, respectively (Figure 8(c)), which are calculated by plotting the positive and negative current density differences at a given potential against the CV scan rates. The triangular Cu@Cu_3P-280 nanorod possesses a higher C_{dl} than Cu/Cu_3P NS since the triangular nanorod structure leads to the high exposure of the surface. This indicates that the formation of nanorod arrays on the nanosheet surface can expose more active sites and promote the reaction kinetics. Moreover, the long-term stability was tested by a constant potential method for 13.5 h, where no significant change in the current was observed (Figure 8(d)). Detailed comparison of triangular Cu@Cu_3P-280 nanorods with other reported Cu_3P electrocatalysts is shown in Table S1, indicating its superior or comparable performance [43−45].

4 Conclusions

In summary, we have successfully prepared

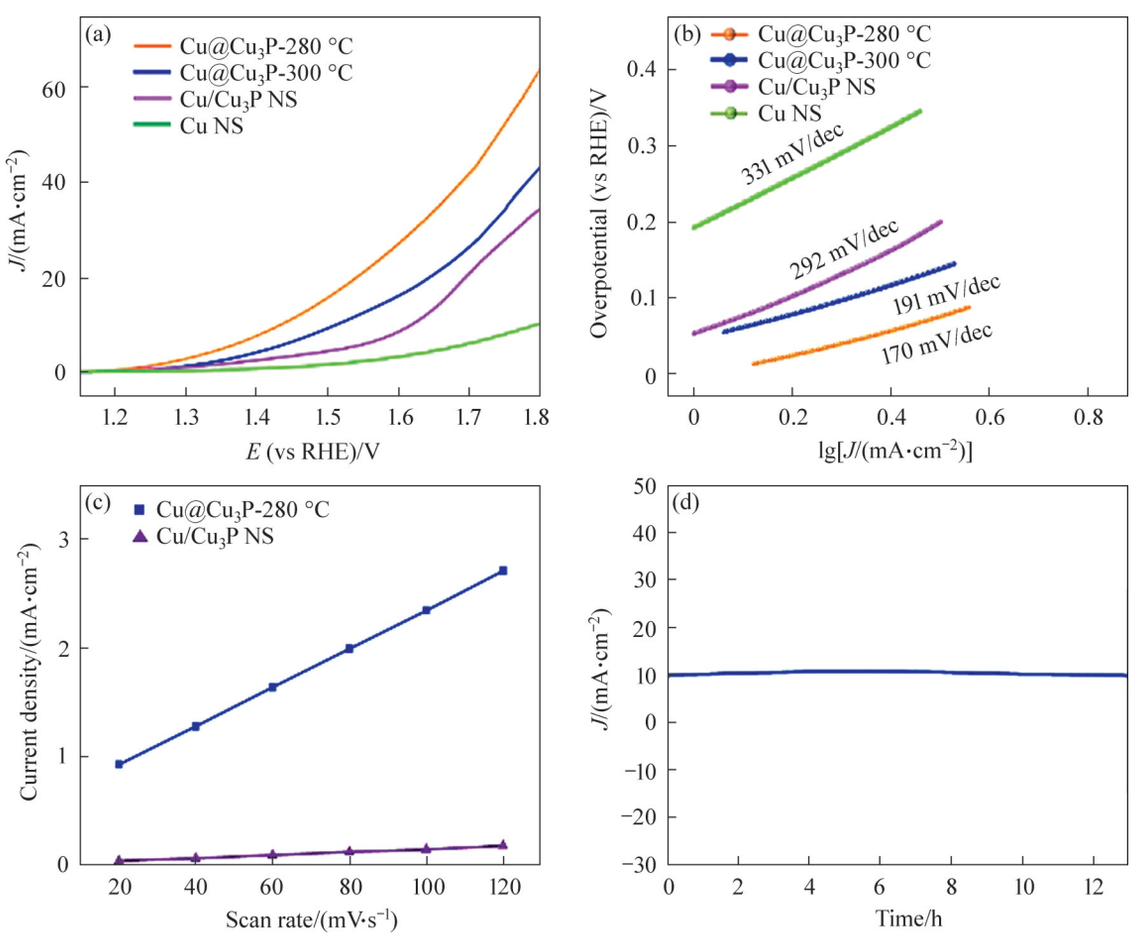

Figure 8 Electrocatalytic activity of the as-prepared triangular Cu@Cu_3P nanorods electrode for OER in 1 mol/L KOH: (a) Polarization curves; (b) Tafel plots; (c) Capacitive current 1.07 V (vs RHE) against the scan rates; (d) Current density curve related to time at 10 mA/cm^2

triangular Cu@Cu_3P nanorod via a facile three-step synthetic strategy, including a hydrothermal synthesis of Cu nanosheet and triangular Cu@CuO nanorod precursor, and a following phosphidation with NaH_2PO_2 in Ar atmosphere. The amount of H_2O_2 and the concentration of NaOH solution have a great influence on the morphology of the product precursor. The catalyst exhibits a high catalytic activity for overall water splitting as a bifunctional catalyst. The enhanced catalytic performance is attributed to the structure and composition of the catalyst. The triangular nanorod provides more active sites owing to the high specific surface area. The triangular Cu@Cu_3P nanorods show good electrical conductivity, benefiting from the substrate of Cu nanosheet which can effectively reduce the resistance of the catalytic system. This triangular Cu@Cu_3P nanorod with enhanced HER and OER electrocatalytic performance and long-term stability might be a promising replacement to the noble metal electrocatalysts in water splitting and fuel cells.

Appendix

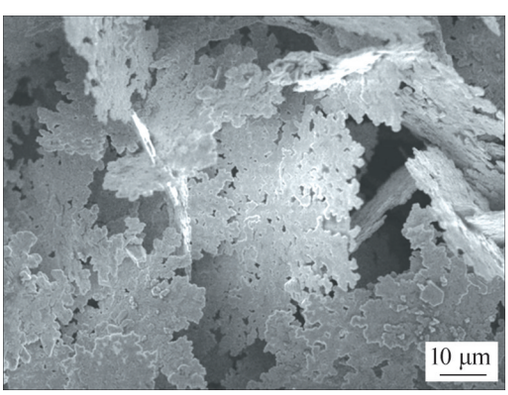

Figure S1 SEM image of Cu nanosheet

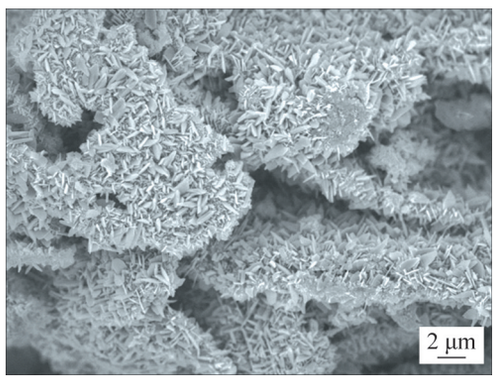

Figure S2 SEM image of triangular Cu@CuO nanorod

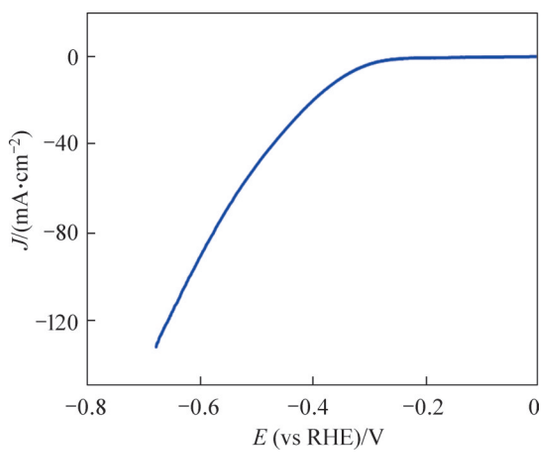

Figure S3 Polarization curve for Cu@CuO/Cu_3P-270 nanorods in 0.5 mol/L H_2SO_4 solution

Contributors

DANG Rui provided the concept and edited the draft of manuscript. DANG Rui and XU Xiu-feng validated the proposed method with practical experiments. XIE Meng-meng accomplished writing-review and editing. All authors have read and agreed to the published version of the manuscript.

Table S1 Comparison of HER and OER catalytic performance of triangular Cu@Cu_3P nanorods and other reported Cu_3P electrocatalysts in acidic and basic conditions

Materials	Electrolyte	Overpotential, η_{onset}/mV	Overpotential, η_{10}/mV	Long-time stability	Ref.
Cu_3P nanocubes	HER in 0.5 mol/L H_2SO_4	145	300	1000 cycles	[43]
Cu_3P NB/Cu	OER in 1 mol/L KOH	320	380	—	[33]
Cu_3P NB/Cu	HER in 0.5 mol/L H_2SO_4	−44	117	9 h (η_{20})	[33]
Cu_3P -450	OER in 1 mol/L KOH	—	290	19 h (1.55 V (vs RHE))	[44]
Cu_3P@C-120	HER in 0.5 mol/L H_2SO_4	51	124	20 h (η_{10})	[45]
Cu_3P@C-120	OER in 1 mol/L KOH	—	300	20 h (η_{10})	[45]
Cu@Cu_3P NR	HER in 0.5 mol/L H_2SO_4	—	252	14 h (η_{10})	This work
Cu@Cu_3P NR	OER in 1 mol/L KOH	—	200	13.5 h (η_{10})	This work

Note: η_{10} and η_{20} are overpotentials under conditions of 20 and 10 mA/cm^2, respectively.

Conflict of interest

DANG Rui, XU Xiu-feng and XIE Meng-meng declare that they have no conflict of interest.

References

[1] WANG Mao-sen, FU Wen-ying, DU Lei, et al. Surface engineering by doping manganese into cobalt phosphide towards highly efficient bifunctional HER and OER electrocatalysis [J]. Applied Surface Science, 2020, 515: 146059. DOI: 10.1016/j.apsusc.2020.146059.

[2] YAN Hai-jing, XIE Ying, WU Ai-ping, et al. Anion-modulated HER and OER activities of 3D Ni-V-based interstitial compound heterojunctions for high-efficiency and stable overall water splitting [J]. Advanced Materials (Deerfield Beach, Fla), 2019, 31(23): e1901174. DOI: 10.1002/adma.201901174.

[3] ALOBAID A, WANG Chun-sheng, ADOMAITIS R A. Mechanism and kinetics of HER and OER on NiFe LDH films in an alkaline electrolyte [J]. Journal of the Electrochemical Society, 2018, 165(15): J3395−J3404. DOI: 10.1149/2.0481815jes.

[4] ENSAFI A A, JAFARI-ASL M, NABIYAN A, et al. Ni_3S_2/ball-milled silicon flour as a bi-functional electrocatalyst for hydrogen and oxygen evolution reactions [J]. Energy, 2016, 116: 392−401. DOI: 10.1016/j.energy.2016.09.128.

[5] JIANG Hao, GU Jin-xing, ZHENG Xu-sheng, et al. Defect-rich and ultrathin N doped carbon nanosheets as advanced trifunctional metal-free electrocatalysts for the ORR, OER and HER [J]. Energy & Environmental Science, 2019, 12(1): 322−333. DOI: 10.1039/C8EE03276A.

[6] SILVA V D, DA SILVA F E F, DE MEDEIROS E S, et al. Catalysts for hydrogen and oxygen evolution reactions (HER/OER) in cells [M]//Heterogeneous Catalysis. Amsterdam: Elsevier, 2022: 457 − 470. DOI: 10.1016/b978-0-323-85612-6.00016-4.

[7] CHENG Jin-bin, ZHANG Hua-min, MA Hai-peng, et al. Study of carbon-supported IrO_2 and RuO_2 for use in the hydrogen evolution reaction in a solid polymer electrolyte electrolyzer [J]. Electrochimica Acta, 2010, 55(5): 1855 − 1861. DOI: 10.1016/j.electacta.2009.10.081.

[8] CHEREVKO S, GEIGER S, KASIAN O, et al. Oxygen and hydrogen evolution reactions on Ru, RuO_2, Ir, and IrO_2 thin film electrodes in acidic and alkaline electrolytes: A comparative study on activity and stability [J]. Catalysis Today, 2016, 262: 170 − 180. DOI: 10.1016/j.cattod.2015.08.014.

[9] WANG Ya-rong, WANG Zhang-jun, JIN Chao, et al. Enhanced overall water electrolysis on a bifunctional perovskite oxide through interfacial engineering [J]. Electrochimica Acta, 2019, 318: 120 − 129. DOI: 10.1016/j.electacta.2019.06.073.

[10] HAO Shao-yun, WANG Ya-hui, ZHENG Guo-kui, et al. Tuning electronic correlations of ultra-small IrO_2 nanoparticles with La and Pt for enhanced oxygen evolution performance and long-durable stability in acidic media [J]. Applied Catalysis B: Environmental, 2020, 266: 118643. DOI: 10.1016/j.apcatb.2020.118643.

[11] SUNG M, KIM J. Oxygen evolution reaction on Pt sphere and Ir-modified Pt sphere electrodes with porous structures [J]. International Journal of Hydrogen Energy, 2018, 43(4): 2130−2138. DOI: 10.1016/j.ijhydene.2017.11.167.

[12] DIAO Fang-yuan, HUANG Wei, CTISTIS G, et al. Bifunctional and self-supported NiFeP-layer-coated NiP rods for electrochemical water splitting in alkaline solution [J]. ACS Applied Materials & Interfaces, 2021, 13(20): 23702 − 23713. DOI: 10.1021/acsami.1c03089.

[13] LUO Shan-shan, WANG Ran, HEI Peng, et al. Self-assembled Ni_2P nanosheet-implanted reduced graphene oxide composite as highly efficient electrocatalyst for oxygen evolution reaction [J]. Colloids and Surfaces A: Physicochemical and Engineering Aspects, 2021, 612: 125992. DOI: 10.1016/j.colsurfa.2020.125992.

[14] SU Zhe, LU Ying-jiong, SRINIVAS K, et al. Carbon nanotubes-interconnected heterostructural FeP/Ni_2P nanospindles as efficient and stable electrocatalysts for oxygen evolution reaction [J]. Journal of Alloys and Compounds, 2021, 883: 160926. DOI: 10.1016/j.jallcom.2021.160926.

[15] YANG Fang, CHEN Xin, LI Zhe, et al. Ultrathin FeP nanosheets as an efficient catalyst for electrocatalytic water oxidation: Promoted intermediates adsorption by surface defects [J]. ACS Applied Energy Materials, 2020, 3(4): 3577−3585. DOI: 10.1021/acsaem.0c00080.

[16] XIONG De-hua, WANG Xiao-guang, LI Wei, et al. Facile synthesis of iron phosphide nanorods for efficient and durable electrochemical oxygen evolution [J]. Chemical Communications, 2016, 52(56): 8711 − 8714. DOI: 10.1039/C6CC04151E.

[17] WANG Ke-wei, TAN Jin-shan, LU Ze-jia, et al. Nanoscale engineering MoP/Fe_2P/RGO toward efficient electrocatalyst for hydrogen evolution reaction [J]. International Journal of Hydrogen Energy, 2018, 43(30): 13939 − 13945. DOI: 10.1016/j.ijhydene.2018.02.012.

[18] JIAO Yan-qing, YAN Hai-jing, WANG Rui-hong, et al. Porous plate-like MoP assembly as an efficient pH-universal hydrogen evolution electrocatalyst [J]. ACS Applied Materials & Interfaces, 2020, 12(44): 49596 − 49606. DOI: 10.1021/acsami.0c13533.

[19] ZHOU Ze-qi, MAHMOOD N, ZHANG Yong-chao, et al. CoP nanoparticles embedded in P and N co-doped carbon as efficient bifunctional electrocatalyst for water splitting [J]. Journal of Energy Chemistry, 2017, 26(6): 1223−1230. DOI: 10.1016/j.jechem.2017.07.021.

[20] ZHUANG Ming-hao, OU Xue-wu, DOU Yu-bing, et al. Polymer-embedded fabrication of Co_2P nanoparticles encapsulated in N, P-doped graphene for hydrogen generation [J]. Nano Letters, 2016, 16(7): 4691−4698. DOI: 10.1021/acs.nanolett.6b02203.

[21] JIN Zhao-yu, LI Pan-pan, XIAO Dan. Metallic Co_2P ultrathin nanowires distinguished from CoP as robust electrocatalysts for overall water-splitting [J]. Green Chemistry, 2016, 18(6): 1459 − 1464. DOI: 10.1039/C5GC02462E.

[22] KIM B K, KIM S K, CHO S K, et al. Enhanced catalytic activity of electrodeposited Ni-Cu-P toward oxygen evolution reaction [J]. Applied Catalysis B: Environmental, 2018, 237: 409−415. DOI: 10.1016/j.apcatb.2018.05.082.

[23] LIU Zi-xuan, WANG Xiao-long, HU Ai-ping, et al. 3D Se-

doped NiCoP nanoarrays on carbon cloth for efficient alkaline hydrogen evolution [J]. Journal of Central South University, 2021, 28(8): 2345−2359. DOI: 10.1007/s11771-021-4774-y.

[24] MONDAL I, MAHATA A, KIM H, et al. A combined experimental and theoretical approach revealing a direct mechanism for bifunctional water splitting on doped copper phosphide [J]. Nanoscale, 2020, 12(34): 17769−17779. DOI: 10.1039/d0nr03414b.

[25] PI Ming-yu, ZHANG Ding-ke, WANG Shu-xia, et al. Enhancing electrocatalytic hydrogen evolution of WP_2 three-dimensional nanowire arrays via Mo doping [J]. Materials Letters, 2018, 213: 315−318. DOI: 10.1016/j. matlet. 2017. 11.058.

[26] NKABINDE S S, MWONGA P V, MPELANE S, et al. Phase-dependent electrocatalytic activity of colloidally synthesized WP and α-WP_2 electrocatalysts for hydrogen evolution reaction [J]. New Journal of Chemistry, 2021, 45(34): 15594−15606. DOI: 10.1039/D1NJ00927C.

[27] LIU Wei, GENG Peng, LI Shi-qing, et al. Tuning electronic configuration of WP_2 nanosheet arrays via nickel doping for high-efficiency hydrogen evolution reaction [J]. Journal of Energy Chemistry, 2021, 55: 17−24. DOI: 10.1016/j.jechem. 2020.06.068.

[28] LIU Wei, GENG Peng, LI Shi-qing, et al. Self-supported three-dimensional WP2 (WP) nanosheet arrays for efficient electrocatalytic hydrogen evolution [J]. International Journal of Hydrogen Energy, 2020, 45(53): 28576−28585. DOI: 10. 1016/j.ijhydene.2020.07.144.

[29] PFEIFFER H, TANCRET F, BICHAT M P, et al. Air stable copper phosphide (Cu_3P): A possible negative electrode material for lithium batteries [J]. Electrochemistry Communications, 2004, 6(3): 263 − 267. DOI: 10.1016/j. elecom.2003.12.012.

[30] WANG Rui, DONG Xi-yan, DU Jiao, et al. MOF-derived bifunctional Cu_3 P nanoparticles coated by a N, P-codoped carbon shell for hydrogen evolution and oxygen reduction [J]. Advanced Materials, 2018, 30(6): 1703711. DOI: 10.1002/adma.201703711.

[31] ZHOU Xin, ZHOU Xiao-liang, LIU Li-min, et al. Self-supported Cu_3P nanowire electrode as an efficient electrocatalyst for the oxygen evolution reaction [J]. RSC Advances, 2021, 11(54): 34137−34143. DOI: 10.1039/D1RA 05526G.

[32] TIAN Jing-qi, LIU Qian, CHENG Ning-yan, et al. Self-supported Cu_3P nanowire arrays as an integrated high-performance three-dimensional cathode for generating hydrogen from water [J]. Angewandte Chemie, 2014, 53(36): 9577−9581. DOI: 10.1002/anie.201403842.

[33] WEI Shu-ting, QI Kun, JIN Zhao, et al. One-step synthesis of a self-supported copper phosphide nanobush for overall water splitting [J]. ACS Omega, 2016, 1(6): 1367 − 1373. DOI: 10.1021/acsomega.6b00366.

[34] DANG Rui, SONG Ling-ling, DONG Wen-jun, et al. Synthesis and self-assembly of large-area Cu nanosheets and their application as an aqueous conductive ink on flexible electronics [J]. ACS Applied Materials & Interfaces, 2014, 6(1): 622−629. DOI: 10.1021/am404708z.

[35] ZHANG Ke, XIONG Zhi-ping, LI Shu-min, et al. Cu_3P/RGO promoted Pd catalysts for alcohol electro-oxidation [J]. Journal of Alloys and Compounds, 2017, 706: 89−96. DOI: 10.1016/j.jallcom.2017.02.179.

[36] HOU Chun-chao, CHEN Qian-qian, WANG Chuan-jun, et al. Self-supported cedarlike semimetallic Cu_3P nanoarrays as a 3D high-performance Janus electrode for both oxygen and hydrogen evolution under basic conditions [J]. ACS Applied Materials & Interfaces, 2016, 8(35): 23037−23048. DOI: 10. 1021/acsami.6b06251.

[37] ZHEN Wen-long, JIAO Wen-jun, WU Yu-qi, et al. The role of a metallic copper interlayer during visible photocatalytic hydrogen generation over a $Cu/Cu_2O/Cu/TiO_2$ catalyst [J]. Catalysis Science & Technology, 2017, 7(21): 5028 − 5037. DOI: 10.1039/C7CY01432E.

[38] FU Zhong-yuan, MA Xin-yi, XIA Bing, et al. Efficient photocatalytic H_2 evolution over Cu and Cu_3P co-modified TiO_2 nanosheet [J]. International Journal of Hydrogen Energy, 2021, 46(37): 19373 − 19384. DOI: 10.1016/j. ijhydene.2021.03.089.

[39] ZHANG Hong-wei, TAN Hui-ru, JAENICKE S, et al. Highly efficient and robust Cu catalyst for non-oxidative dehydrogenation of ethanol to acetaldehyde and hydrogen [J]. Journal of Catalysis, 2020, 389: 19−28. DOI: 10.1016/j. jcat.2020.05.018.

[40] LIN Jia, ZENG Cheng-hui, LIN Xiao-ming, et al. CNT-assembled octahedron carbon-encapsulated Cu_3P/Cu heterostructure by in situ MOF-derived engineering for superior lithium storage: Investigations by experimental implementation and first-principles calculation [J]. Advanced Science (Weinheim, Baden-Wurttemberg, Germany), 2020, 7(14): 2000736. DOI: 10.1002/advs.202000736.

[41] KOU Yu-li, WANG Kang-kang, WUMAER M, et al. Synthesis of hollow $Cu@Cu_{3-x}P$ core-shell nanostructure as dual-functional catalyst with copper vacancy for enhancing chemical reduction and photocatalytic performance [J]. Applied Surface Science, 2022, 589: 153031. DOI: 10.1016/j. apsusc.2022.153031.

[42] LI Xiao-lin, ZHANG Jia-ling, ZHANG Yu, et al. Copper induced phosphide for enhanced electrochemical hydrogen evolution reaction [J]. International Journal of Hydrogen Energy, 2020, 45(41): 21422 − 21430. DOI: 10.1016/j. ijhydene.2020.05.213.

[43] MA Lian-bo, SHEN Xiao-ping, ZHOU Hu, et al. Synthesis of Cu_3P nanocubes and their excellent electrocatalytic efficiency for the hydrogen evolution reaction in acidic solution [J]. RSC Advances, 2016, 6(12): 9672−9677. DOI: 10.1039/C5RA24427G.

[44] HAO Jin-hui, YANG Wen-shu, HUANG Zhi-peng, et al. Superhydrophilic and superaerophobic copper phosphide microsheets for efficient electrocatalytic hydrogen and oxygen evolution [J]. Advanced Materials Interfaces, 2016, 3(16): 1600236. DOI: 10.1002/admi.201600236.

[45] RONG Jian, XU Jin-chao, QIU Feng-xian, et al. Sea urchin-like MOF-derived formation of porous $Cu_3P@C$ as an efficient and stable electrocatalyst for oxygen evolution and hydrogen evolution reactions [J]. Advanced Materials Interfaces, 2019, 6(14): 1900502. DOI: 10.1002/admi.2019 00502.

(Edited by FANG Jing-hua)

中文导读

铜纳米片表面磷化铜三角纳米柱的构筑及其电催化分解水研究

摘要：开发能够取代贵金属的高效、廉价、稳定的非贵金属催化剂，对于推动电催化水裂解析氢、析氧技术的发展具有重要意义。本文以铜纳米片为模板和导电基底，H_2O_2为氧源，NaOH为pH调节剂，通过原位氧化的方法在Cu纳米片表面构筑三角柱状结构的Cu@CuO；再对Cu@CuO进行低温磷化，获得三角纳米柱状Cu@Cu_3P。实验结果表明，磷化温度在调节Cu@Cu_3P纳米柱阵列的形貌、组成及活性位点数量方面具有显著效果。当磷化温度为280 ℃时，可获得形貌均一、活性高的纳米三角柱状阵列结构材料(Cu@Cu_3P-280)。Cu@Cu_3P-280电极在0.5 mol/L H_2SO_4电解质中表现出良好的析氢催化活性，在电流密度为10 mA/cm^2时，其过电位为252 mV，催化14 h后，电流密度仍可达初始值的72%。Cu@Cu_3P-280电极在1 mol/L KOH电解质中也展现出优异的催化析氧活性，当电流密度为10 mA/cm^2时，其过电位仅为200 mV，催化12 h后，电流密度保持初始值的93%。此研究为可持续、低价、双功能电催化材料的定向设计与制备提供理论基础。

关键词：Cu@Cu_3P；电催化；析氢反应；析氧反应